ADVANCED FUNCTIONAL MATERIALS
www.afm-journal.de



# Multiplexed Nondiffracting Nonlinear Metasurfaces

*Zhi Li, Wenwei Liu, Guangzhou Geng, Zhancheng Li, Junjie Li, Hua Cheng,* Shuqi Chen,* and Jianguo Tian*

**Metasurfaces and planar photonic nanostructures have drawn great interest from the optical scientific community due to their diverse abilities of manipulating electromagnetic waves and high integration. Most metasurfaces launch diffracting waves, and thus suffer from divergence, short working distance, and instability. Although much effort has been devoted to researching nondiffracting metasurfaces which can launch electromagnetic waves with constant transverse intensity profiles in free-space propagation, the number of working channels is inherently limited as these meta-devices are implemented in the linear optical regime. Here, the multiplexed nondiffracting nonlinear metasurfaces are theoretically proposed and experimentally realized, which can generate the representative nondiffracting Bessel beam and Airy beam. Three Bessel beams with different numerical apertures and topological charges and three Airy beams with different propagation curves and focal lengths can be generated by a combination of different spins and wavelengths. The complex properties of the nondiffracting beams can be designed and detected in a more comprehensive and concise way with Fourier analysis. This proof-of-concept represents a new strategy for realizing multiplexed nondiffracting metasurfaces with advantages of ultracompactness, high-pixelation, and easy integration and paves the way for multi-channel optical communication and manipulation.**

## 1. Introduction

In optics, the beam-like fields can propagate without diffraction as spatial solitons or waveguide modes in nonlinear materials or waveguides, respectively. In 1987, Durnin et al. discovered Bessel beams and extended the term nondiffracting beam to the propagation in vacuum,[1] which revived the interest in the diffraction of light and stimulated the emergence of a new research direction to deal with the localized transfer of electromagnetic energy. Bessel beams are a set of exact solutions to the homogeneous Helmholtz equation, and the transverse intensity profiles of such beams can be described by the Bessel functions of the first kind. This discovery inspired the thoughts of exploring nondiffracting beams by finding solutions to the Helmholtz equation. Due to the mathematical similarity between the paraxial Helmholtz equation and the Schrödinger equation, the concept of the Airy wave packet predicted by Berry and Balazs within the context of quantum mechanics was introduced into the field of optics,[2] and the nondiffracting Airy beam was demonstrated for the first time by Siviloglou et al.[3,4] Both types of the nondiffracting beams mentioned above have the nondiffracting and self-healing properties. Airy beam also has the remarkable feature of self-accelerating without any external potential. Due to these unique natures, nondiffracting beams have attracted spectacular interest and have application prospects in optical tweezer,[5,6] spectral broadening,[7,8] high-resolution light-sheet microscopy,[9] and curved plasma channels.[10] The conventional approaches for generating nondiffracting beams still have some defects, which limit further application of such beams. The numerical aperture (NA) of the Bessel beam generated by an axicon is limited, and using a lens paired with an annular aperture suffers from low efficiency. Besides, an additional phase-modulating element is required to generate higher-order Bessel beams. For the generation of Airy beams, the combination of a spatial light modulator (SLM) and the Fourier transform system is still the most common approach.[4,11,12] However, the large pixel size of SLMs limits the generation of Airy beams with both high spatial resolution and precision. Moreover, the bulky Fourier transform system poses a challenge for implementing Airy beams in a compact integrated optics platform.

With the rapid development of modern fabrication techniques, manipulation of electromagnetic (EM) waves with

Dr. Z. Li, Dr. W. Liu, Dr. G. Geng, Dr. Z. Li, Prof. H. Cheng, Prof. S. Chen, Prof. J. Tian
The Key Laboratory of Weak Light Nonlinear Photonics
Ministry of Education
School of Physics and TEDA Institute of Applied Physics
Nankai University
Tianjin 300071, China
E-mail: hcheng@nankai.edu.cn; schen@nankai.edu.cn

Dr. G. Geng, Prof. J. Li
Beijing National Laboratory for Condensed Matter Physics
Institute of Physics
Chinese Academy of Sciences
Beijing 100190, China

Prof. S. Chen
Renewable Energy Conversion and Storage Center
Nankai University
Tianjin 300071, China

Prof. S. Chen
The Collaborative Innovation Center of Extreme Optics
Shanxi University
Taiyuan, Shanxi 030006, China

Prof. S. Chen
Collaborative Innovation Center of Light Manipulations and Applications
Shandong Normal University
Jinan 250358, China

The ORCID identification number(s) for the author(s) of this article can be found under https://doi.org/10.1002/adfm.201910744.

**DOI: 10.1002/adfm.201910744**

 

integrated planar optical systems has become possible. Metasurfaces consisting of customized planar nanostructures have become a research hotspot due to their ability of providing a platform for arbitrarily manipulating EM waves at the subwavelength scale.[13–15] Benefiting from all kinds of the strong light–matter interactions, various compact optical elements based on metasurfaces have been proposed including ultrathin flat metalenses,[16–18] optical holograms,[19,20] planar wave plates,[21–23] and so on. However, these diffracting metasurfaces cannot realize applications that have strict requirements for suppressing the diffraction of EM waves, such as axial imaging[9] and high density EM wave array for optical interconnection.[24] In contrast, nondiffracting metasurfaces are capable of launching EM waves with robustness and low divergence. Despite recent attempts at realizing nondiffracting metasurfaces, these works were implemented in the linear optical regime, where the number of the information channels is inherently limited.[25–31] The recent extension of metasurfaces to nonlinear optical regime has proved that the information storage capacity of individual metasurface can be greatly enhanced by the generation of higher harmonics.[32–37] The multiplexed nondiffracting metasurfaces can be realized by combination of the nonlinear optical processes. Meanwhile, it is hard to fully describe the properties of the nondiffracting beams only in real space due to the high degree of complexity of nondiffracting beams.

Here, we theoretically propose and experimentally demonstrate the multiplexed nondiffracting nonlinear metasurfaces which can be classified into another broad category compared with the previous multiplexed diffracting metasurfaces to lift the aforementioned restrictions, and provide a platform for launching multiplexed Bessel beams and Airy beams. Three Bessel beams with different NAs and topological charges (higher-order Bessel beams), and three Airy beams with different propagation curves and focal lengths (abruptly autofocusing Airy beams) can be generated by combination of different spins and wavelengths. We also demonstrate the Fourier analysis of nondiffracting beams which can describe the complex properties of such beams in a more comprehensive and concise way compared with the previous real space analysis. More specifically, the properties of nondiffracting beams can be described by detecting the focal plane of the lens used for Fourier transform instead of measuring the entire beam propagation. We envision this multiplexed nondiffracting metalauncher would promise great applications in optical communication, multilayered cell manipulation, and large field-of-view bioimaging.[38]

## 2. Results and Discussion

In order to realize multiplexed nondiffracting metasurfaces, we adopt the meta-atoms with onefold (C1) rotational symmetry. According to the selection rules and nonlinear Pancharatnam–Berry (P–B) phase elements of harmonic generations from a fundamental wave with circularly polarized state $\sigma$,[32,33] two second harmonic generation (SHG) processes with same ($\sigma$) and opposite ($-\sigma$) polarization states to that of fundamental wave are allowed. The nonlinear P–B phases of these two SHG signals with different spins $\sigma$ and $-\sigma$ are $\sigma\theta$ and $3\sigma\theta$, respectively, where $\theta$ is the in-plane orientation angle of each meta-atom. Therefore, one linear ($2\sigma\theta$) and two SHG ($\sigma\theta$ and $3\sigma\theta$) P–B phases corresponding to the optical signals of different wavelengths and spins can be generated by introducing SHG processes. It is worth noting that these three P–B phases are linearly related as originating from the same element.

In order to generate a zeroth-order Bessel beam, the meta-axicon needs to refract all the incident light by the same angle $\alpha_0$ at the design wavelength $\lambda_0$. Thus, a radial phase profile is required:

$$\varphi_0(r) = k_0 r \cdot \mathrm{NA}_0 \tag{1}$$

where $k_0 = \frac{2\pi}{\lambda_0}$ is the linear wave vector, $r = \sqrt{x^2 + y^2}$ is the distance of each meta-atom from the origin of the coordinate, $\mathrm{NA}_0 = \sin\alpha_0$ and $\alpha_0$ can be expressed as $\alpha_0 = \tan^{-1}\left(\frac{r}{\mathrm{DOF}_0}\right)$, where DOF is the depth of focus. When we study the signal of $n$th harmonic generation, Equation (1) can be rewritten as $\phi_n(r) = k_n r \cdot NA_n$, where $\varphi_n(r) = \frac{n \pm 1}{2}\varphi_0(r)$, $k_n = nk_0$ is the nonlinear wave vector and $\mathrm{NA}_n$ is the nonlinear numerical aperture. Thus, the relation between linear and nonlinear NAs is

$$\mathrm{NA}_n = \frac{n \pm 1}{2n}\mathrm{NA}_0 \tag{2}$$

Therefore, the SHG Bessel beams with spin $\sigma$ and $-\sigma$ have nonlinear NAs of $\mathrm{NA}_0/4$ and $3\mathrm{NA}_0/4$, respectively. For the generation of a higher-order Bessel beam, an addition phase profile of a vortex plate $l\Phi$ is required, where $l$ represents the topological charge and $\Phi$ is the azimuthal angle ($\Phi = \arctan\left(\frac{y}{x}\right)$ when $x > 0$, and $\Phi = \pi + \arctan\left(\frac{y}{x}\right)$ when $x < 0$), and Equation (1) becomes

$$\varphi_0(r) = k_0 r \cdot \mathrm{NA}_0 + l_0\Phi \tag{3}$$

Thus the phase angle continually increases anticlockwise along a closed loop from 0 to $2\pi l$ and returns to the origin, where the angle zero is exactly equal to $2\pi l$, forming a continuous phase distribution along the closed loop. According to nonlinear P–B phase elements, we obtain the relation between linear and nonlinear phase profiles as $\varphi_{V0} = 2\varphi_{Vn1}(\sigma) = 2\varphi_{Vn2}/3\ (-\sigma)$. When we set the topological charge $l_0 = 2$ for the linear Bessel beam, we can easily get the topological charges $l_{n1} = 1$ and $l_{n2} = 3$ for the SHG Bessel beams with spin $\sigma$ and $-\sigma$, respectively. The radius of the metasurfaces is 80 μm and the linear NA is set as 0.53 (corresponding to a linear DOF of 127 μm). Based on the aforementioned analysis, one linear Bessel beam ($-\sigma$) with $\mathrm{NA}_0 = 0.53$ ($\mathrm{DOF}_0 = 127$ μm), $l_0 = 2$, two nonlinear Bessel beams with $\mathrm{NA}_{n1} = 0.4$ ($\mathrm{DOF}_{n1} = 183$ μm), $l_{n1} = 3$ ($-\sigma$) and $\mathrm{NA}_{n2} = 0.13$ ($\mathrm{DOF}_{n2} = 595$ μm), $l_{n2} = 1$ ($\sigma$) can be simultaneously generated, as shown in **Figure 1**a. The insets show the interference patterns of the Bessel beams.

The multiplexed nondiffracting metasurfaces which can launch Airy beams are also realized by introducing the nonlinear signals. The Airy beams in linear frequency have been realized with nondiffracting metasurfaces by phase modulation or phase and amplitude co-modulation of each meta-atom.[29–31]

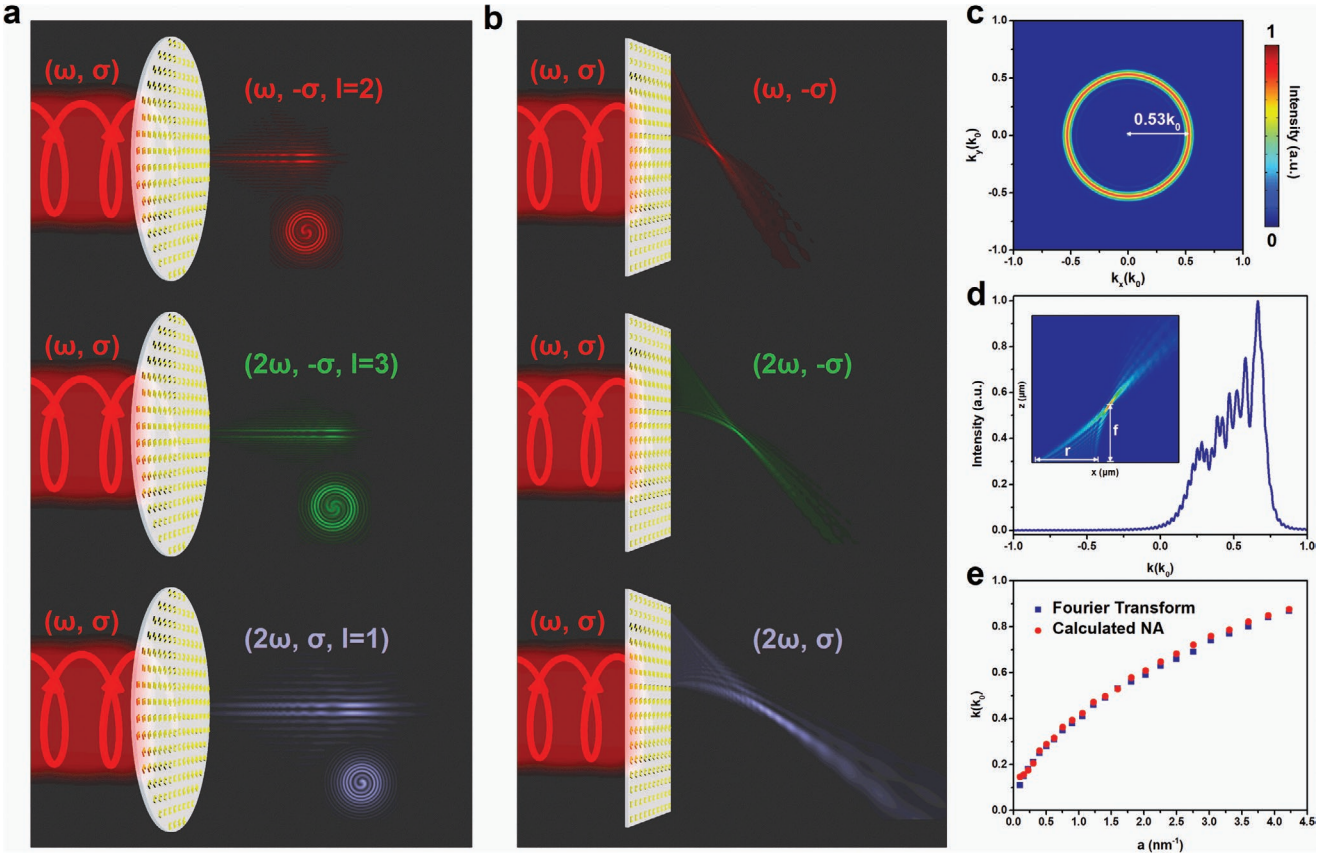


**Figure 1.** Designs of the multiplexed nondiffracting nonlinear metasurfaces. a) With different combination of spins and wavelengths, three Bessel beams with different DOFs and topological charges can be generated simultaneously. The insets show the interference patterns of the Bessel beams. b) With different combination of spins and wavelengths, three Airy beams with different propagation trajectories can be generated simultaneously. c) The numerical intensity cross profile in *k*-space of the linear Bessel beam with the NA of 0.53. d) The numerical intensity cross profile in *k*-space of the linear Airy beam with an acceleration coefficient $a_0 = 2.5$ nm$^{-1}$. The inset shows the numerical intensity distribution of such beam in real space. e) The calculated NAs and peak positions in *k*-space.

In order to ensure the maximum SHG conversion efficiency, the resonance wavelength of each meta-atom needs to fit the excitation wavelength. We adopt only phase modulation to generate the multiplexed Airy beams. The Airy function can be well approximated as $\mathrm{Ai}(x) \approx x^{-\frac{1}{4}} \exp\left(iCx^{\frac{3}{2}}\right)$, where $C$ is a constant.[2] The amplitude of this equation decreases with $x$, for simplicity, the amplitude term is usually ignored and only the phase modulation is considered to generate the Airy beams.[39] This method was later confirmed to be equivalent to the Legendre transformation of optical caustics of the Airy beams.[40] Since the caustic of the 1D Airy beam yields the parabolic path $y = a_0x^2$, the corresponding phase function after the Legendre transformation is

$$\varphi_0 = -\frac{4}{3} a_0^{\frac{1}{2}} k_0 x^{\frac{3}{2}} \tag{4}$$

where $a_0$ is the acceleration coefficient. Utilizing the same analytical method, the relation between linear and nonlinear acceleration coefficients is

$$a_n^{\frac{1}{2}} = \frac{n \pm 1}{n^2} a_0^{\frac{1}{2}} \tag{5}$$

Therefore, the SHG Airy beams with spin $\sigma$ and $-\sigma$ propagate along the caustic trajectories of $y = a_0x^2/16$ and $y = 9a_0x^2/16$, respectively. As illustrated in Figure 1b, one linear and two SHG Airy beams with different propagation trajectories can be generated simultaneously. The linear acceleration coefficient is set to be $a_0 = 2.5$ nm$^{-1}$.

In order to design and detect the multiplexed nondiffracting metasurfaces more comprehensively and simply, we also analyze the launched beams in *k*-space. For the Bessel beams, the NAs and DOFs of such beams are unverifiable in real space but easy to be verified in *k*-space. The intensity distribution of a Bessel beam in *k*-space can be obtained by Fourier transformation of Equation (1):

$$F(k) = \sqrt{2\pi}\delta(k - k_0 \cdot \mathrm{NA}) \tag{6}$$

The above equation represents that the Fourier transformation of a Bessel beam becomes the Dirac delta function. Thus, the intensity distribution in *k*-space is a ring with a radius of $k_0 \cdot \mathrm{NA}$. Figure 1c represents the Fourier plane image of the linear zeroth-order Bessel beams. The radius of the ring is independent of the topological charge of the Bessel beam, therefore it is also known as perfect optical vortex.[41,42] Thus, by detecting the intensity distribution of a Bessel beam in *k*-space,

one can confirm its NA and further infer the DOF in a simple and accurate way.

For the Airy beams, it is essential to locate the position with peak intensity in the design process, since many applications of such beams can benefit from it, such as abruptly auto-focusing Airy beams.[43,44] However, the design in real space can only control the propagation trajectory of the beam but cannot locate this position. The position of peak intensity for an Airy beam can be located with Fourier analysis. Comparing the Airy beam to a half lens, the position of peak intensity is the focus with a focal length $f$. The Airy beam has its own NA defined as $\mathrm{NA} = \sin\left(\arctan\left(\frac{r}{f}\right)\right)$, and conforms well to the peak position of the highest peak in $k$-space after Fourier transformation, as shown in Figure 1d. The calculated NAs and peak positions in $k$-space are presented in Figure 1e. The computed correlation coefficient between them reaches a strong correlative value of 0.9992, and the maximum error between them does not exceed 5%. Therefore, the NA and focal length of the Airy beam can be obtained with Fourier analysis during the design process, and the deflection offset can be further calculated by the propagation trajectory to locate the position of the focus. Besides, the position of the focus can also be easily located by the intensity distribution in $k$-space during the detection process. The setup used to measure the nondiffracting beams in $k$-space is shown in **Figure 2**a.

Since the split ring resonators (SRRs) meet the C1 rotational symmetry requirement and possess high SHG conversion efficiency, we select the gold SRRs as meta-atoms. Although gold does not possess intrinsic bulk second-order nonlinearity due to its centrosymmetric atomic lattice as per the electric dipole approximation, the surface of gold can support the SHG since electrons at the surface reside in a non-symmetric environment and can therefore avoid the symmetry constraints. As the extensively investigated nanostructures in SHG process, the SRRs have been proven to greatly enhance the SHG efficiency by exciting the magnetic resonances.[45,46] Therefore, the waveband of the magnetic resonance is designed to fit the excitation wavelength around 1550 nm. To optimize the response wavelength of the SRRs, 3D finite-difference time-domain (FDTD) approach was performed. In the theoretical simulations, a gold SRR is placed on silica substrate with periodic boundary conditions and the period is 400 nm in both $x$- and $y$-directions, light is illuminated from the substrate side and perfectly matched layers are used at the bottom of the air domain. The complex dielectric constants of gold and silica substrate are taken from measured data.[47] The optimized SRR can be characterized by four geometrical parameters: length of long arm $L_x$, length of short arm $L_y$, width $w$, and thickness $h$ of the nanoantenna. The simulated transmission spectra for horizontal (solid blue line) and vertical (solid red line) polarized incident light of uniformly arranged SRRs are shown in Figure 2b, where the magnetic-dipole mode excited by horizontal polarized component is located at 1560 nm. To experimentally realize the multiplexed zeroth-order and higher-order Bessel beams, two metasurfaces consisting of gold SRRs were fabricated using electron beam

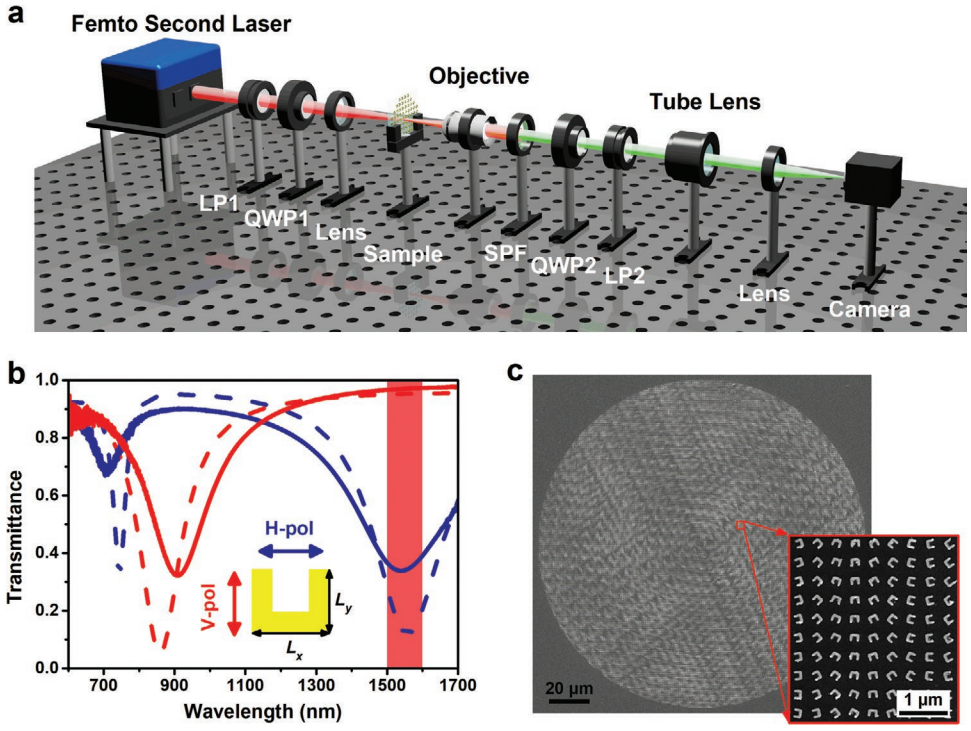


**Figure 2.** Experimental setup and fabrication of the multiplexed nondiffracting nonlinear metasurfaces. a) Illustration of the measurement setup for measuring the intensity distributions of multiplexed Bessel beams in $k$-space. LP, linear polarizer; QWP, quarter-wave plate; SPF, short-pass filter. b) Simulated (dashed lines) and measured (solid lines) transmission spectra for horizontal and vertical polarized incident light of uniformly arranged SRRs. Length of long arm $L_x$, short arm $L_y$, width $w$ and thickness $h$ of the nanoantenna are 185, 155, 40, and 35 nm, respectively. c) SEM micrograph of the fabricated metasurface realizing multiplexed higher-order Bessel beam.

lithography (EBL). The scanning electron microscopy (SEM) images of the sample of higher-order Bessel beam are shown in Figure 2c. In contrast to the simulated results, the measured transmission spectra (dashed lines) of a reference sample containing uniformly arranged SRRs are also displayed in Figure 2b. As expected before, the sample has a magnetic-dipole mode around 1540 nm, which is slightly blue-shifted compared with the designed result, thus the strongest SHG process will occur near the excitation wavelength.

We first demonstrated the multiplexed zeroth-order Bessel beams. A custom-built setup was used to characterize both linear and SHG Bessel beams; the objective, tube lens, and camera were all integrated on a XYZ translation stage to scan the intensity profiles of the nondiffracting beams along *z*-direction. (Figure S4, Supporting Information). Under left-handed circular polarized (LCP, $\sigma$) illumination, the linear Bessel beam has an opposite spin ($-\sigma$) to that of incidence. A quarter-wave plate (QWP) and a linear polarizer (LP) were placed in front of the camera to filter out any co-polarized light. As presented in **Figure 3**a, the measured intensity distribution along the propagation direction clearly reveals the nondiffracting property of Bessel beam during propagation. Figure 3b shows the intensity

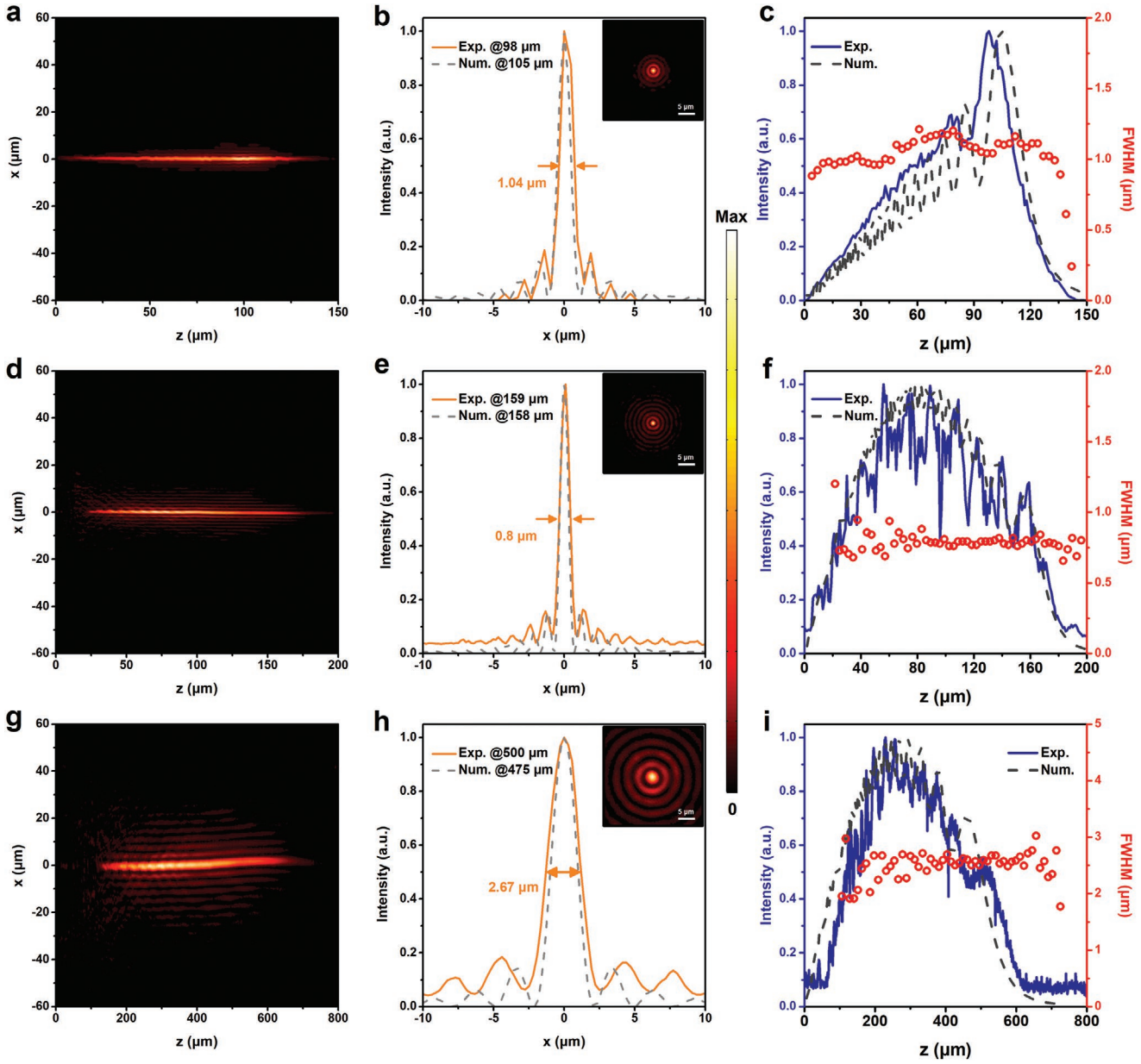


**Figure 3.** Experimental demonstration of the multiplexed zeroth-order Bessel beams. Measured intensity distributions along the propagation direction of a) linear and SHG Bessel beams with spin d) $-\sigma$ and g) $\sigma$. The numerical and measured intensity cross profiles of b) linear and SHG Bessel beams with spin e) $-\sigma$ and h) $\sigma$ at focal planes, the insets show the intensity distributions at focal planes. The numerical and measured intensity distributions and the measured FWHMs at different planes along the direction of propagation of c) linear and SHG Bessel beams with spin f) $-\sigma$ and i) $\sigma$. The scale bar is adapted for each figure.

cross profile at the focal plane of Bessel beam. The measured (orange solid line) full width at half maximum (FWHM) is observed to be 1.04 μm, which agrees well with theoretical limit of 1.04 μm (Part S1, Supporting Information). The inset indicates the transverse intensity profile at the corresponding plane. To further verify the propagation and nondiffracting characteristics, we detected the intensity distribution and the FWHM at different planes along the direction of propagation, as shown in Figure 3c. The measured (blue solid line) and numerical (grey dashed line) intensity distributions both present a typical profile of the Bessel beam generated by an axicon,[48] which prove that the meta-axicon indeed replaces the traditional axicon. Meanwhile, the FWHM of the Bessel beam remains stable (from 0.8 to 1.2 μm) throughout the whole process of propagation and does not expand. When the DOF is exceeded, the FWHM appears to have a significant fluctuation due to the weak intensity of the beam. Similar to the linear Bessel beam, the nonlinear Bessel beams with same ($\sigma$) and opposite ($-\sigma$) circular polarization state to that of the incidence can be selectively detected by turning a QWP and an LP placed in front of the camera. The measured intensity profile of the SHG Bessel beam with spin $-\sigma$ along the propagation direction is presented in Figure 3d, which also reveals the nondiffracting nature of the beam. As shown in Figure 3e, the measured intensity cross profile at the focal plane indicates that the FWHM is about 0.80 μm, which generally agrees with its theoretical value of 0.69 μm. The intensity distribution along the direction of propagation deviates from the expected one (the waist of the Gaussian beam was set as 70 μm in the numerical calculation), as presented in Figure 3f. This phenomenon is due to the fact that the incident light is focused before exciting the nonlinear Bessel beam, thus the SHG signal from edge of the sample is weaker than that from center. The interference of these weak signals forms the latter part of the Bessel beam along the propagation direction. However, the FWHM of the Bessel beam still remains stable (from 0.6 to 0.9 μm) throughout the whole process of propagation. For the SHG Bessel beam with spin $\sigma$, the measured intensity profile along the propagation direction is indicated in Figure 3g. Due to the FWHM is inversely proportional to NA, a roughly tripled FWHM of 2.67 μm to its opposite spin counterpart is observed as shown in Figure 3h. This phenomenon can also be verified through the transverse intensity profile (inset of Figure 3h). The FWHM of the Bessel beam also remains stable (from 2.2 to 2.8 μm) as presented in Figure 3i. Noticeably, the nonlinear Bessel beams have better security and no background noise originated from the illumination. The background noise in the experimental measurement comes from the dark current noise of the scientific complementary metal-oxide-semiconductor (sCMOS) camera.

We next measured the multiplexed higher-order Bessel beams. As illustrated in Figure 1a, in addition to having different NAs, these three Bessel beams have different topological charges. The measured intensity distribution along the propagation direction of the linear higher-order Bessel beam is shown in **Figure 4**a. The nondiffracting property and the intensity singularity can be clearly observed. As presented in Figure 4b, the measured intensity cross profile at the focal plane indicates that the diameter of the doughnut-shaped intensity profile is about 2.82 μm, which agrees well with its theoretical value of 2.85 μm and the intensity distribution (inset of Figure 4b) further confirms the intensity singularity. The intensity distribution along the direction of propagation is similar to the zeroth-order Bessel beam and the diameter of the annular ring of the Bessel beam remains stable (from 2.3 to 2.9 μm) throughout the whole process of propagation as shown in Figure 4c. To verify the topological charge of the linear higher-order Bessel beam, partial co-polarized light was deliberately reserved by turning the LP as a reference wave. The two petals of the experimental interference pattern (Figure 4d) unambiguously validate $l_0 = 2$. The measured intensity distributions along the propagation direction and the measured intensity cross profiles at the focal planes of the SHG higher-order Bessel beams with spin $-\sigma$ and $\sigma$ are shown in Figure 4e,f,i,j, respectively. The diameters of annular rings of the Bessel beams at the focal planes are 2.64 and 3.60 μm, which are both a bit larger than the theoretically expected 2.60 and 3.41 μm. Besides, the diameters of annular rings of the Bessel beams also both remain stable (from 2.1 to 2.9 μm and from 3 to 4.2 μm) as presented in Figure 4g,k, respectively. The topological charge of an ultrafast laser beam is hard to be quantified due to the ultrashort coherence length of it. To overcome this difficulty, we adopted a simplified interferometry based on ±1 order phase mask and these two orders create a self-interference pattern, thus the topological charge can be recognized by the interferogram (Figure S5, Supporting Information). Three branches ($-\sigma$) and one branch ($\sigma$), appearing in the measured fringe patterns as shown in Figure 4h,l, confirm the presence of phase defects at the cores of these two beams and ensure that the SHG higher-order Bessel beams carry topological charges of $l_{n1} = 3$ and $l_{n2} = 1$, respectively.

To verify the NAs and DOFs of multiplexed Bessel beams, we further detected such beams in *k*-space. As shown in Figure 2a, a lens was adopted behind the tube lens to realize Fourier transform of the nondiffracting beams at its focal plane. **Figure 5**a,d represents the Fourier plane images of the linear zeroth-order and higher-order Bessel beams. The measured NAs are both about 0.54, which agree well with the design and above analysis. The center bright spot is the uncoupled light that does not contribute to the formation of Bessel beams, which is also the original point of *k*-space. Due to the practical Bessel beam being spatially limited and an approximation of ideal Bessel beam within a finite region, the ring in *k*-space has a certain width. Due to the fact that the amplitude term does not enter the Dirac delta function after Fourier transformation, the intensity distribution of the illumination does not affect the radii of the rings of SHG Bessel beams. As shown in the Fourier plane images of SHG Bessel beams with spin $-\sigma$ (Figure 5b,e) and $\sigma$ (Figure 5c,f), the zeroth-order and higher-order SHG Bessel beams possess the same NAs of 0.41 and 0.13, respectively. The zeroth-order spots in the centers of SHG Bessel beams are much weaker than those of the linear ones, since no background noise is derived from the illumination.

We next measured the multiplexed Airy beams in both real space and *k*-space in **Figure 6**. The measured intensity distribution along the propagation direction reveals the nondiffracting (near the focus) and self-accelerating properties of Airy beam during propagation in Figure 6a. In order to more accurately demonstrate the properties of the Airy beam, we quantitatively characterized its propagation trajectory in Figure 6b. The

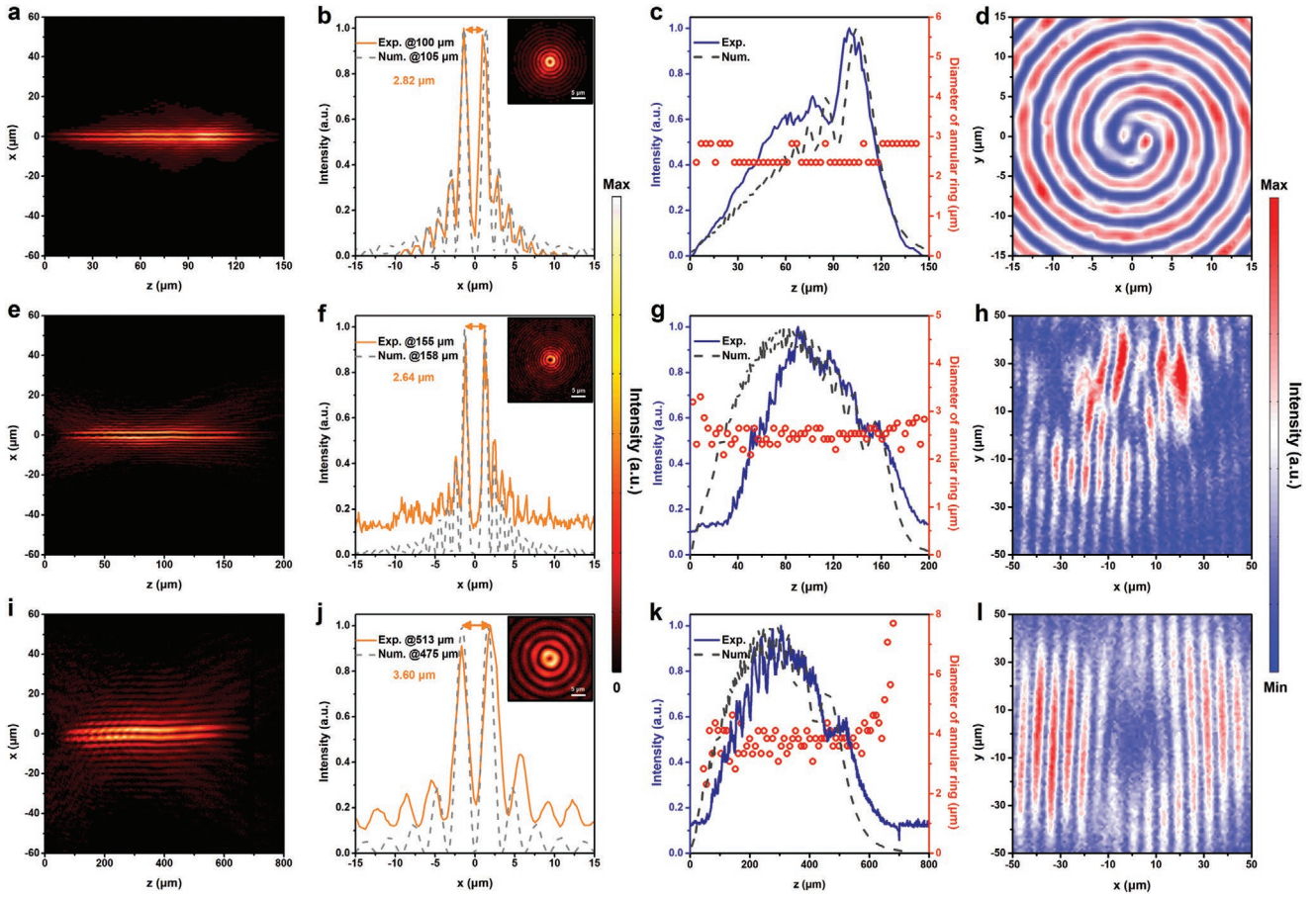


**Figure 4.** Experimental demonstration of the multiplexed higher-order Bessel beams. Measured intensity distributions along the propagation direction of a) linear and SHG Bessel beams with spin e) $-\sigma$ and i) $\sigma$. The numerical and measured intensity cross profiles of b) linear and SHG Bessel beams with spin f) $-\sigma$ and j) $\sigma$ at focal planes, the insets show the intensity distributions at focal planes. The numerical and measured intensity distributions and the measured diameters of the annular rings at different planes along the direction of propagation of c) linear and SHG Bessel beams with spin g) $-\sigma$ and k) $\sigma$. Measured interference patterns of d) linear and SHG Bessel beams with spin h) $-\sigma$ and l) $\sigma$. The scale bars are adapted for each figure.

deflection (blue triangles) and FWHM (red circles) of the main lobe were extracted from the experimental results. Strong variation of the FWHM occurs at the initial stage of propagation due to the loss of amplitude information. However, the FWHM remains relatively stable (around 3 μm, between the white dashed lines) in the nondiffracting zone up to a distance of approximately $30\lambda_0$, which is marked by grey shading. Outside this zone, the main lobe expands quickly and the nondiffracting nature of the Airy beam gradually fades out. Similar to the FWHM, the deflection of the main lobe has an obvious deviation from the theoretical trajectory ($y = 2.5\ \mathrm{nm}^{-1}x^2$) at the initial stage. However, the main lobe follows a smooth trajectory which fits well the theoretical caustic in the nondiffracting zone. The theoretical trajectory is offset considering the instability of the deflection at the initial stage of propagation. To locate the position of the focus, we detected the intensity distribution of the Airy beam in *k*-space, whose cross profile is shown in Figure 6c. The peak position indicates the linear Airy beam possess a NA of 0.65, which agrees well with both the design value of 0.66 and the experimental value extracted from the real space of 0.65. The measured intensity distributions along the propagation direction of the SHG Airy beams with spin $-\sigma$ and $\sigma$ are shown in Figure 6d,g, respectively. Consistent with the linear Airy beam, the FWHMs of the main lobes of the SHG Airy beams with spin $-\sigma$ and $\sigma$ both have variations at the initial stage of propagation and remain stable (around 5 and 6 μm) in the nondiffracting zones ($218\lambda_{SHG}$ and $513\lambda_{SHG}$), as shown in Figure 6e,h. Meanwhile, deflections of the main lobes also agree well with the theoretical caustics ($y = 22.5\ \mathrm{nm}^{-1}x^2/16$ and $y = 2.5\ \mathrm{nm}^{-1}x^2/16$ for spin $-\sigma$ and $\sigma$) in the nondiffracting zones. The reason for the abrupt change in the deflections and FWHMs of the main lobes is that it is hard to distinguish the boundary of the main lobes when the intensity of the SHG Airy beam is too weak, thus the side lobes may be merged into the main lobes. The SHG Airy beams have longer diffracting zones due to the lower NAs and larger signal-to-noise ratio compared with the linear counterpart. The intensity cross profiles of the SHG Airy beams with spin $-\sigma$ and $\sigma$ in *k*-space are presented in Figure 6f,i. The obtained NAs of 0.49 and 0.14 with Fourier analysis conformed well to both the design values of 0.49 and 0.15, and the experimental value extracted from the real space of 0.49 and 0.13, respectively.

An abruptly auto-focusing beam is an accelerating beam which suddenly generates a focus and the intensity of the

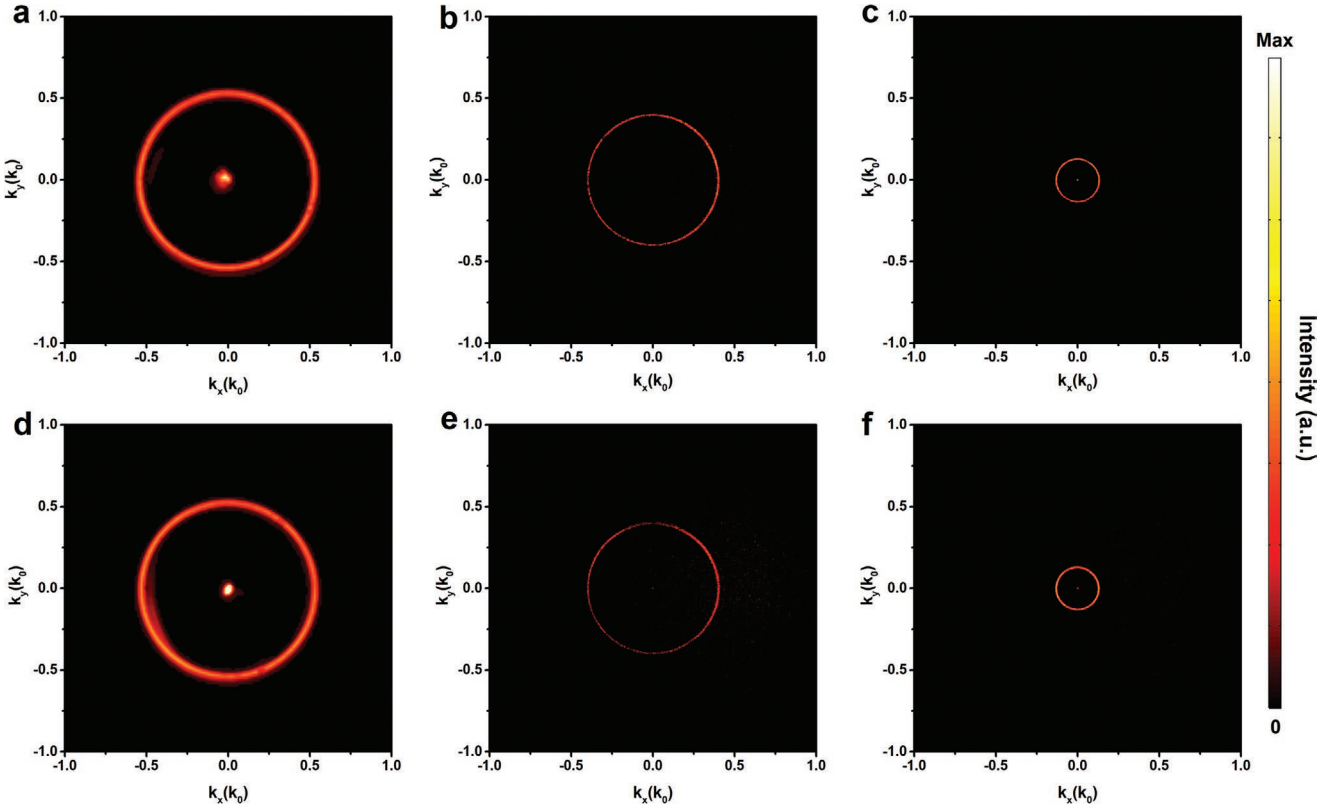


**Figure 5.** Experimental demonstration of the multiplexed Bessel beams in *k*-space. Measured intensity distributions of the multiplexed zeroth-order a) linear and SHG Bessel beams with spin b) $-\sigma$ and c) $\sigma$ in *k*-space. Measured intensity distributions of the multiplexed higher-order d) linear and SHG Bessel beams with spin e) $-\sigma$ and f) $\sigma$ in *k*-space. The scale bar is adapted for each figure.

beam remains almost constant during the previous propagation. Such beams are highly desirable in many applications, such as in biological laser treatments, they can only operate on the intended area without damaging other tissues. Abruptly auto-focusing beams also have the ability of self-healing compared with the conventional lens focusing. The most common abruptly auto-focusing beams rely on two symmetrical Airy beams.[43,44] The interference of their main lobes leads to a localized field enhancement, thus it is important to locate the foci of the Airy beams in addition to the propagation trajectories of them. According to the calculated intensity distributions in *k*-space, the deflections of the foci of linear and SHG Airy beams are 10.14, 13.95 ($-\sigma$), and 19.58 ($\sigma$) μm, respectively. Due to the lower NA of the SHG Airy beam with spin $\sigma$, the main lobe has a longer DOF. Thus the interval between the two Airy beams is taken as 22 μm to ensure that the linear and SHG ($-\sigma$) Airy beams have ideal abruptly auto-focusing phenomena. The measured intensity distribution and the maximum intensity along the propagation direction of the linear abruptly auto-focusing Airy beam are shown in **Figure 7**a,b. It is obvious that the maximum intensity remains at low levels until the focus. As presented in Figure 7c, the measured intensity cross profile at the focal plane indicates that a retrieved FWHM is about 1.27 μm. The intensity cross profile in *k*-space indicates two symmetrical Airy beams as shown in Figure 7d. Thus one can directly analyze the position of focus instead of scanning the entire intensity distribution in real space. The measured intensity distributions and maximum intensities along the propagation direction of the SHG abruptly auto-focusing Airy beams with spin $-\sigma$ and $\sigma$ are shown in Figure 7e,f,i,j, respectively. According to the design principle discussed above, the SHG signal with spin $-\sigma$ performs an obvious abruptly auto-focusing phenomenon. Meanwhile, the orthogonally polarized signal can still focus. The smaller FWHM of the SHG abruptly auto-focusing Airy beams with spin $-\sigma$ at the focal plane also confirms this result, as shown in Figure 7g,k. The intensity cross profiles in *k*-space indicate two pairs of symmetrical Airy beams with different NAs of the SHG signals with spin $-\sigma$ and $\sigma$, as shown in Figure 7h,l.

## 3. Conclusion

In conclusion, we have theoretically proposed and experimentally demonstrated multiplexed nondiffracting nonlinear metasurfaces which can be classified into another broad category compared with the previous multiplexed diffracting metasurfaces and provided a platform for the generation of multiplexed Bessel beams and Airy beams. Three Bessel beams with different NAs and topological charges (higher-order Bessel beams), and three Airy beams with different caustic trajectories and focal lengths (abruptly auto-focusing Airy beams) can be generated by different metasurfaces. Each nondiffracting beam can only be read out by specific combination of spins

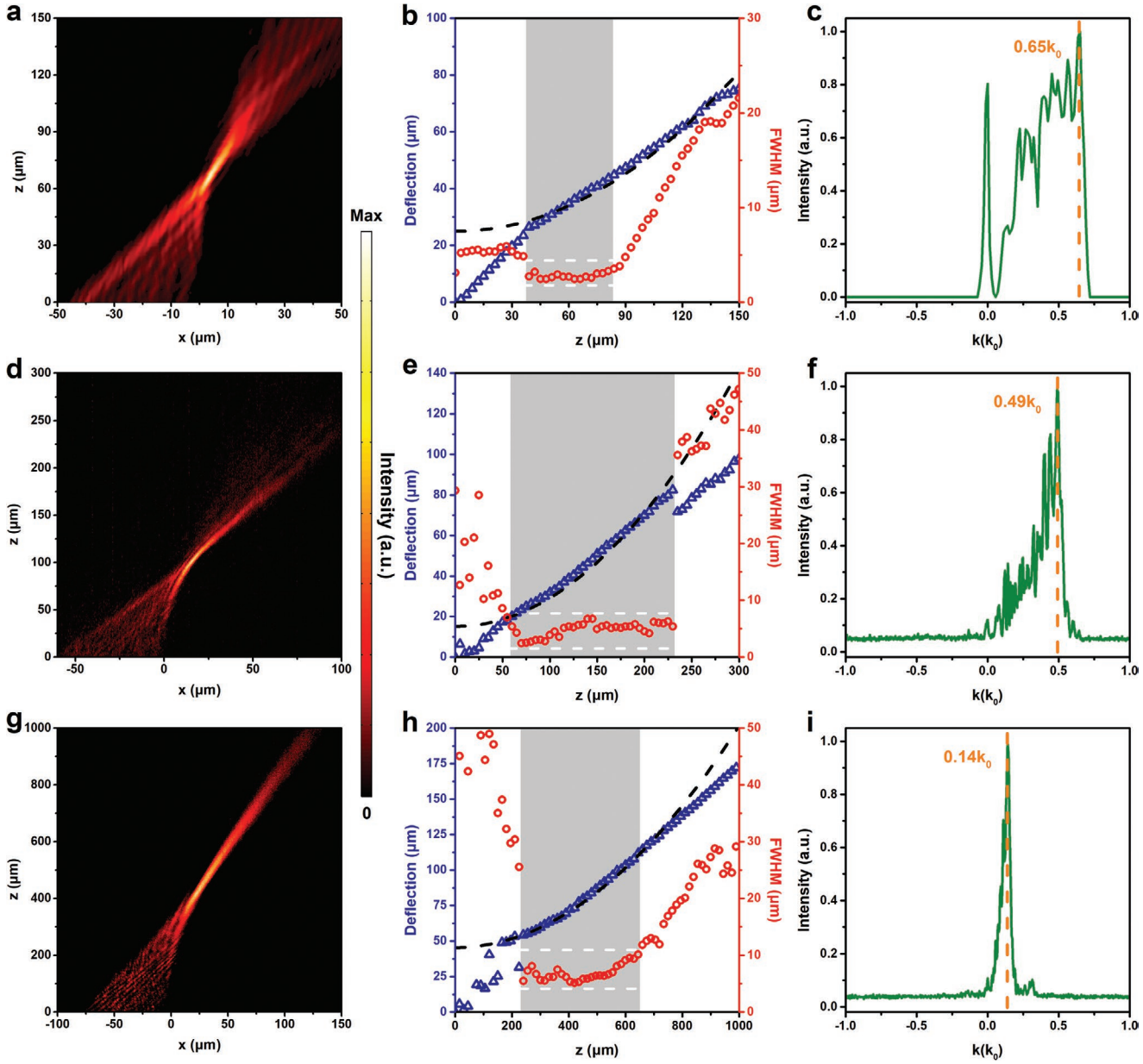


**Figure 6.** Experimental demonstration of the multiplexed Airy beams. Measured intensity distributions along the propagation direction of a) linear and SHG Airy beams with spin d) $-\sigma$ and g) $\sigma$. Measured deflections and FWHMs of the main lobes at different planes along the direction of propagation of b) linear and SHG Airy beams with spin e) $-\sigma$ and h) $\sigma$. Measured intensity cross profiles in $k$-space of c) linear and SHG Airy beams with spin f) $-\sigma$ and i) $\sigma$.

and wavelengths. We also demonstrated that the properties of the nondiffracting beams can be designed and detected in a more comprehensive and concise way with Fourier analysis. Furthermore, this method can be easily generalized to accelerating beams following other caustic trajectories, such as natural logarithmic and biquadratic caustic trajectories. Although the SHG conversion efficiency of the SRR we used is only on the order $10^{-12}$, it can be further enhanced by adopting hybrid metasurfaces,[49,50] multi-quantum-wells-based metasurfaces,[51] and metasurfaces consist of novel nonlinear materials, such as semiconductors and perovskites.[52,53] The multiplexed nondiffracting nonlinear metasurfaces have the potential to be applied in multi-channel light-sheet microscopy which can simultaneously image infrared and visible light without changing the infrared light source. Besides, such metasurfaces can also open new avenues for optical communication in harsh environment, and multi-channel optical manipulation. The number of working channels can be even further extended by introducing other nonlinear processes or integrating with active metasurfaces.[54,55] The design and detection strategy can effectively reduce the complexity of analyzing nondiffracting beams.

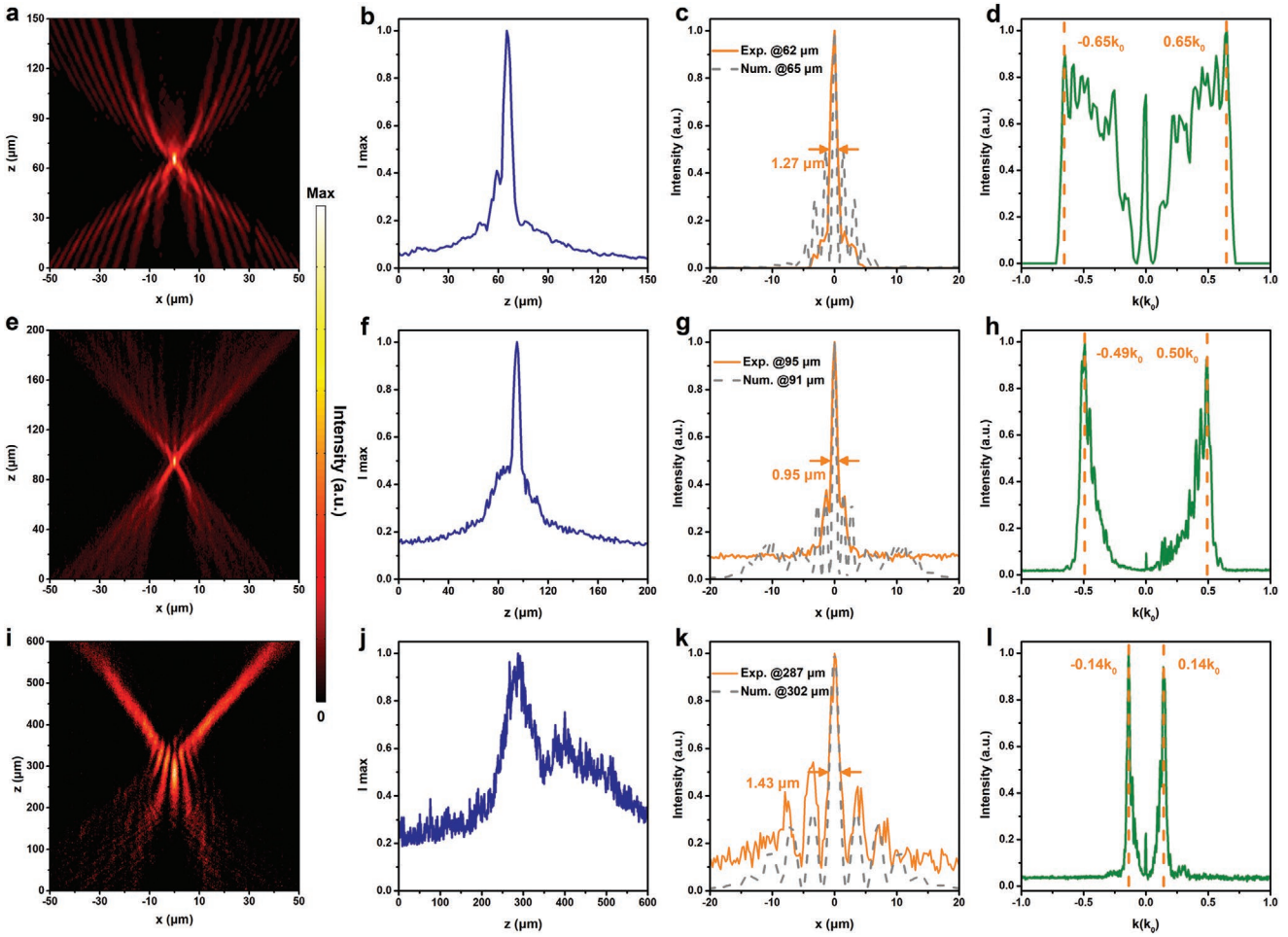


**Figure 7.** Experimental demonstration of the multiplexed abruptly auto-focusing Airy beams. Measured intensity distributions along the propagation direction of a) linear and SHG abruptly auto-focusing Airy beams with spin e) $-\sigma$ and i) $\sigma$. Measured maximum intensities along the propagation direction of b) linear and SHG abruptly auto-focusing Airy beams with spin f) $-\sigma$ and j) $\sigma$. The numerical and measured intensity cross profiles of c) linear and SHG abruptly auto-focusing Airy beams with spin g) $-\sigma$ and k) $\sigma$ at focal planes. Measured intensity cross profiles in $k$-space of d) linear and SHG abruptly auto-focusing Airy beams with spin h) $-\sigma$ and l) $\sigma$.

## 4. Experimental Section

*Sample Fabrication*: The sample was prepared using a standard electron beam lithography and a lift-off process. First, a layer of poly(methyl methacrylate; PMMA) with thickness of 120 nm and a layer of poly(3,4-ethylenedioxythiophene) polystyrene sulfonate (Pedot:PSS) with thickness of 35 nm were spin-coated on the fused silica substrate by sequence. The Pedot:PSS layer was intended for charge release during the EBL process which employed a 100 kV voltage, 200 pA current, and 1000 μC cm$^{-2}$ dose. After defining the nanometer scale metasurface patterns by the EBL process, the Pedot:PSS layer was removed with pure water for 60 s and PMMA was developed with methyl isobutyl ketone (MIBK)/iso propyle alcohol (IPA) (3:1) for 40 s. Then a 2 nm Cr layer and a 35 nm Au layer were deposited on the resist by sequence with electron beam evaporation deposition (EBD) method. Then the Cr film was striped by removing PMMA with hot acetone at degree of 60 °C for 20 min, leaving the metal pattern on substrate. The Cr layer here aimed to enhance adhesion between the silica surface and the gold layer.

*Measurement Procedure*: An Erbium-doped ultrafast fiber laser (Toptica Photonics AG FemtoFiber Pro NIR, repetition frequency: 80 MHz, pulse length: ≈80 fs) centered at 1550 nm was coupled to a home-built microscopy. An LP and a QWP were combined to generate the incident circularly polarized light, the metasurface was illuminated at normal incidence and the generated linear and nonlinear nondiffracting beams were filtered by another combination of a QWP and an LP, then collected with an objective, a tube lens, and a scientific camera. The objective, tube lens (Thorlabs ITL200), and camera were all integrated on a XYZ translation stage to scan the intensity profiles of the nondiffracting beams with a step of 1 μm along $z$-direction. For linear measurement, an average power of 1 mW, a 50 × objective (SIGMA-KOKI PAL-50-NIR-HR-LC00 50 × NA = 0.67) and an InGaAs camera (HAMAMATSU InGaAs C10633) were used, the lens and short-pass filters are removed. For nonlinear measurement, the fundamental pulses had an average power of 350 mW and were focused to a spot with a diameter of ≈160 μm (by a lens with focal length of 200 mm). A 50 × objective, a 20 × objective (SIGMA-KOKI PAL-20-NIR-HR-LC00 20 × NA = 0.45) and an sCMOS camera (HAMAMATSU ORCA-Flash4.0 V3) were used for collecting the SHG signals with spin $-\sigma$ and $\sigma$, respectively. For the measurement of topological charges of SHG higher-order Bessel beams, a ±1 order phase mask (made of JGS1, with period of 18 μm, depth of 0.87 μm) was placed behind the tube lens, and a lens (with focal length of 75 mm) was used to amplify the imaging. For the measurement of the nondiffracting beams in $k$-space, a lens was adopted behind the tube lens to realize Fourier transform of the nondiffracting beams at its focal

plane, which was also imaged by the InGaAs camera (linear signal) or sCMOS camera (SHG signal).

## Supporting Information

Supporting Information is available from the Wiley Online Library or from the author.

## Acknowledgements

This work was supported by the National Key Research and Development Program of China (2016YFA0301102 and 2017YFA0303800), the National Natural Science Fund for Distinguished Young Scholar (11925403) the Ministry of Science and Technology of China (2016YFA0200803 and 2016YFA0200402), the National Natural Science Foundation of China (11974193, 11904181, 11904183, 91856101, and 11774186), Natural Science Foundation of Tianjin for Distinguished Young Scientists (18JCJQJC45700), and the National Postdoctoral Program for Innovative Talents (BX20180148).

## Conflict of Interest

The authors declare no conflict of interest.

## Keywords

fourier analysis, nondiffracting beams, nondiffracting metasurfaces, Pancharatnam–Berry phase, second harmonic generation

Received: December 27, 2019
Revised: March 11, 2020
Published online:

[1] J. Durnin, J. J. Miceli, J. H. Eberly, *Phys. Rev. Lett.* **1987**, *58*, 1499.
[2] M. V. Berry, N. L. Balazs, *Am. J. Phys.* **1979**, *47*, 264.
[3] G. A. Siviloglou, D. N. Christodoulides, *Opt. Lett.* **2007**, *32*, 979.
[4] G. A. Siviloglou, J. Broky, A. Dogariu, D. N. Christodoulides, *Phys. Rev. Lett.* **2007**, *99*, 213901.
[5] J. Baumgartl, M. Mazilu, K. Dholakia, *Nat. Photonics* **2008**, *2*, 675.
[6] K. Dholakia, T. Čižmár, *Nat. Photonics* **2011**, *5*, 335.
[7] A. Dubietis, P. Polesana, G. Valiulis, A. Stabinis, P. Di Trapani, A. Piskarskas, *Opt. Express* **2007**, *15*, 4168.
[8] P. Polynkin, M. Kolesik, J. Moloney, *Phys. Rev. Lett.* **2009**, *103*, 123902.
[9] T. Vettenburg, H. I. C. Dalgarno, J. Nylk, C. Coll-Lladó, D. E. K. Ferrier, T. Čižmár, F. J. Gunn-Moore, K. Dholakia, *Nat. Methods* **2014**, *11*, 541.
[10] P. Polynkin, M. Kolesik, J. V. Moloney, G. A. Siviloglou, D. N. Christodoulides, *Science* **2009**, *324*, 229.
[11] G. A. Siviloglou, J. Broky, A. Dogariu, D. N. Christodoulides, *Opt. Lett.* **2008**, *33*, 207.
[12] Y. Hu, P. Zhang, C. Lou, S. Huang, J. Xu, Z. Chen, *Opt. Lett.* **2010**, *35*, 2260.
[13] N. Yu, P. Genevet, M. A. Kats, F. Aieta, J.-P. Tetienne, F. Capasso, Z. Gaburro, *Science* **2011**, *334*, 333.
[14] X. Ni, N. K. Emani, A. V. Kildishev, A. Boltasseva, V. M. Shalaev, *Science* **2012**, *335*, 427.
[15] X. Yin, Z. Ye, J. Rho, Y. Wang, X. Zhang, *Science* **2013**, *339*, 1405.
[16] X. Chen, L. Huang, H. Mühlenbernd, G. Li, B. Bai, Q. Tan, G. Jin, C.-W. Qiu, S. Zhang, T. Zentgraf, *Nat. Commun.* **2012**, *3*, 1198.
[17] M. Khorasaninejad, W. T. Chen, R. C. Devlin, J. Oh, A. Y. Zhu, F. Capasso, *Science* **2016**, *352*, 1190.
[18] W. Liu, Z. Li, H. Cheng, C. Tang, J. Li, S. Zhang, S. Chen, J. Tian, *Adv. Mater.* **2018**, *30*, 1706368.
[19] L. Huang, X. Chen, H. Mühlenbernd, H. Zhang, S. Chen, B. Bai, Q. Tan, G. Jin, K.-W. Cheah, C.-W. Qiu, J. Li, T. Zentgraf, S. Zhang, *Nat. Commun.* **2013**, *4*, 2808.
[20] G. Zheng, H. Mühlenbernd, M. Kenney, G. Li, T. Zentgraf, S. Zhang, *Nat. Nanotechnol.* **2015**, *10*, 308.
[21] S. Kruk, B. Hopkins, I. I. Kravchenko, A. Miroshnichenko, D. N. Neshev, Y. Kivshar, *APL Photonics* **2016**, *1*, 030801.
[22] P. C. Wu, W.-Y. Tsai, W. T. Chen, Y.-W. Huang, T.-Y. Chen, J.-W. Chen, C. Y. Liao, C. H. Chu, G. Sun, D. P. Tsai, *Nano Lett.* **2017**, *17*, 445.
[23] Z. Liu, Z. Li, Z. Liu, H. Cheng, W. Liu, C. Tang, C. Gu, J. Li, H.-T. Chen, S. Chen, J. Tian, *ACS Photonics* **2017**, *4*, 2061.
[24] C. Yu, M. R. Wang, A. J. Varela, B. Chen, *Opt. Commun.* **2000**, *177*, 369.
[25] F. Aieta, P. Genevet, M. A. Kats, N. Yu, R. Blanchard, Z. Gaburro, F. Capasso, *Nano Lett.* **2012**, *12*, 4932.
[26] D. Lin, P. Fan, E. Hasman, M. L. Brongersma, *Science* **2014**, *345*, 298.
[27] M. Pu, X. Li, X. Ma, Y. Wang, Z. Zhao, C. Wang, C. Hu, P. Gao, C. Huang, H. Ren, X. Li, F. Qin, J. Yang, M. Gu, M. Hong, X. Luo, *Sci. Adv.* **2015**, *1*, e1500396.
[28] W. T. Chen, M. Khorasaninejad, A. Y. Zhu, J. Oh, R. C. Devlin, A. Zaidi, F. Capasso, *Light: Sci. Appl.* **2017**, *6*, e16259.
[29] Z. Li, H. Cheng, Z. Liu, S. Chen, J. Tian, *Adv. Opt. Mater.* **2016**, *4*, 1230.
[30] E.-Y. Song, G.-Y. Lee, H. Park, K. Lee, J. Kim, J. Hong, H. Kim, B. Lee, *Adv. Opt. Mater.* **2017**, *5*, 1601028.
[31] Q. Fan, W. Zhu, Y. Liang, P. Huo, C. Zhang, A. Agrawal, K. Huang, X. Luo, Y. Lu, C. Qiu, H. J. Lezec, T. Xu, *Nano Lett.* **2019**, *19*, 1158.
[32] S. Chen, G. Li, F. Zeuner, W. H. Wong, E. Y. B. Pun, T. Zentgraf, K. W. Cheah, S. Zhang, *Phys. Rev. Lett.* **2014**, *113*, 033901.
[33] G. Li, S. Chen, N. Pholchai, B. Reineke, P. W. H. Wong, E. Y. B. Pun, K. W. Cheah, T. Zentgraf, S. Zhang, *Nat. Mater.* **2015**, *14*, 607.
[34] W. Ye, F. Zeuner, X. Li, B. Reineke, S. He, C.-W. Qiu, J. Liu, Y. Wang, S. Zhang, T. Zentgraf, *Nat. Commun.* **2016**, *7*, 11930.
[35] Z. Li, W. Liu, Z. Li, C. Tang, H. Cheng, J. Li, X. Chen, S. Chen, J. Tian, *Laser Photonics Rev.* **2018**, *12*, 1800164.
[36] M. Ma, Z. Li, W. Liu, C. Tang, Z. Li, H. Cheng, J. Li, S. Chen, J. Tian, *Laser Photonics Rev.* **2019**, *13*, 1900045.
[37] Y. Chen, X. Yang, J. Gao, *Adv. Opt. Mater.* **2018**, *6*, 1800646.
[38] W. Liu, Z. Li, H. Cheng, S. Chen, J. Tian, *Phys. Rev. Appl.* **2017**, *8*, 014012.
[39] D. M. Cottrell, J. A. Davis, T. M. Hazard, *Opt. Lett.* **2009**, *34*, 2634.
[40] L. Froehly, F. Courvoisier, A. Mathis, M. Jacquot, L. Furfaro, R. Giust, P. A. Lacourt, J. M. Dudley, *Opt. Express* **2011**, *19*, 16455.
[41] P. Vaity, L. Rusch, *Opt. Lett.* **2015**, *40*, 597.
[42] S. Fu, T. Wang, C. Gao, *J. Opt. Soc. Am. A* **2016**, *33*, 1836.
[43] N. K. Efremidis, D. N. Christodoulides, *Opt. Lett.* **2010**, *35*, 4045.
[44] D. G. Papazoglou, N. K. Efremidis, D. N. Christodoulides, S. Tzortzakis, *Opt. Lett.* **2011**, *36*, 1842.
[45] M. W. Klein, C. Enkrich, M. Wegener, S. Linden, *Science* **2006**, *313*, 502.
[46] K. O'Brien, H. Suchowski, J. Rho, A. Salandrino, B. Kante, X. Yin, X. Zhang, *Nat. Mater.* **2015**, *14*, 379.
[47] E. D. Palik, *Handbooks of Optical Constants of Solids*, Academic Press, New York **1998**.

[48] D. McGloin, K. Dholakia, *Contemp. Phys.* **2005**, *46*, 15.
[49] H. Linnenbank, Y. Grynko, J. Förstner, S. Linden, *Light: Sci. Appl.* **2016**, *5*, e16013.
[50] Z. Li, W. Liu, Z. Li, H. Cheng, S. Chen, J. Tian, *Opt. Lett.* **2017**, *42*, 3117.
[51] J. Lee, M. Tymchenko, C. Argyropoulos, P.-Y. Chen, F. Lu, F. Demmerle, G. Boehm, M.-C. Amann, A. Alù, M. A. Belkin, *Nature* **2014**, *511*, 65.
[52] S. Liu, M. B. Sinclair, S. Saravi, G. A. Keeler, Y. Yang, J. Reno, G. M. Peake, F. Setzpfandt, I. Staude, T. Pertsch, I. Brener, *Nano Lett.* **2016**, *16*, 5426.
[53] F. Timpu, A. Sergeyev, N. R. Hendricks, R. Grange, *ACS Photonics* **2017**, *4*, 76.
[54] L. Cong, P. Pitchappa, C. Lee, R. Singh, *Adv. Mater.* **2017**, *29*, 1700733.
[55] L. Cong, P. Pitchappa, Y. Wu, L. Ke, C. Lee, N. Singh, H. Yang, R. Singh, *Adv. Opt. Mater.* **2017**, *5*, 1600716.